RSC Advances

PAPER

View Article Online
View Journal | View Issue

Cite this: RSC Adv., 2014, 4, 42454

Modeling of thermocapillary flow to purify single-walled carbon nanotubes

Jizhou Song,†*[a] Chaofeng Lu,†[b] Chenxi Zhang,[c] Sung Hun Jin,[d] Yuhang Li,[e] Simon N. Dunham,[f] Xu Xie,[f] Frank Du,[f] Yonggang Huang*[g] and John A. Rogers[f]

Received 29th July 2014
Accepted 29th August 2014

DOI: 10.1039/c4ra08895f

www.rsc.org/advances

Single walled carbon nanotubes (SWNTs) are of significant interest in the electronic materials research community due to their excellent electrical properties. The mixture of synthesized SWNTs, however, significantly hampers device performance, particularly for potential applications in digital electronics. Recent purification techniques involve successful and complete removal of metallic SWNTs from horizontal arrays by using thermocapillary flows in thin film resists initiated by selective Joule heating. In this paper, an analytical model, as well as a fully coupled thermo-mechanical-fluid finite element model, is developed to study the physics of thermocapillary flow in this context. A simple scaling law for the film thickness profile is established in terms of the geometry (*e.g.*, film thickness), material (*e.g.*, thermal conductivity and viscosity) and loading parameters (*e.g.*, power density). The results show that the normalized thickness profile only depends on three non-dimensional parameters in addition to the normalized position and normalized time. In particular, for the experimentally investigated system, the thickness profile only depends on a single non-dimensional parameter. These findings may serve as useful design guidelines for process optimization.

Published on 04 September 2014. Downloaded by Zhejiang University on 12/09/2014 01:10:14.

1. Introduction

Owing to their exceptional electrical properties such as high carrier mobilities and current switching ratios,[1–3] single-walled carbon nanotubes (SWNTs) remain of high interest in the electronic materials research community for applications in logic transistors/circuits,[4–10] radiofrequency transistors,[11–16] optoelectronic devices[17–19] and sensors.[20–22] The ideal configuration of SWNTs in electronics involves horizontally aligned arrays of purely semiconducting SWNTs, as parallel transport pathways from source to drain with effective performance that greatly exceeds that of randomly oriented SWNTs due to absence of tube-to-tube junctions.[2,23] A main challenge is that SWNTs grow as mixtures of both metallic and semiconducting tubes using standard techniques; this heterogeneity in SWNT properties frustrates their practical application to electronics.

Existing techniques for creating horizontally aligned arrays of purely semiconducting SWNTs fall into two categories. The first, including ultracentrifugation,[24,25] chromatography[26–28] and others, is to purify the SWNTs and then assemble them into arrays. These approaches have been shown to provide capabilities in yielding s-SWNTs in arrays, but the resulting s-SWNTs are typically short, chemically coated and assembled with low degrees of alignment.[29–32] The second is to produce the SWNTs in arrays with nearly perfect alignment (>99.9% of SWNTs within 0.01° of the preferred growth direction) through chemical vapor deposition (CVD) based growth on quartz substrates[23,33] and then to purify them. Various techniques based on electrical,[34] chemical[35–37] or optical[38] effects offer some ability to remove metallic SWNTs (m-SWNTs) to overcome this challenge and show promises, but none can approach the purity requirements for applications in modern digital electronics (>99.9999% s-SWNTs).[39]

Recently, Jin *et al.*[40] introduced a purification technique referred as thermocapillary enabled purification (TcEP) to enable complete, large-scale elimination of m-SWNTs with the ability to meet and even exceed these purity requirements. Fig. 1 shows a schematic illustration of the purification process. A partial top-gate transistor structure is fabricated on SWNT arrays grown on quartz substrates. Uniform thermal

[a]Department of Engineering Mechanics and Soft Matter Research Center, Zhejiang University, Hangzhou 310027, China. E-mail: jzsong@zju.edu.cn

[b]Department of Civil Engineering and Soft Matter Research Center, Zhejiang University, Hangzhou 310058, China

[c]Department of Mechanical and Aerospace Engineering, University of Miami, Coral Gables, Florida 33146, USA

[d]Department of Electronics Engineering, Incheon National University, Incheon, 406-772, Republic of Korea

[e]The Solid Mechanics Research Center, Beihang University (BUAA), Beijing 100191, China

[f]Department of Materials Science and Engineering, Frederick Seitz Materials Research Laboratory, University of Illinois at Urbana-Champaign, Urbana, Illinois 61801, USA

[g]Department of Civil and Environmental Engineering, Department of Mechanical Engineering, Center for Engineering and Health and Skin Desease Research Center, Northwestern University, Evanston, Illinois, 60208, USA. E-mail: y-huang@northwestern.edu

† These authors contributed equally to this work.

 This journal is © The Royal Society of Chemistry 2014

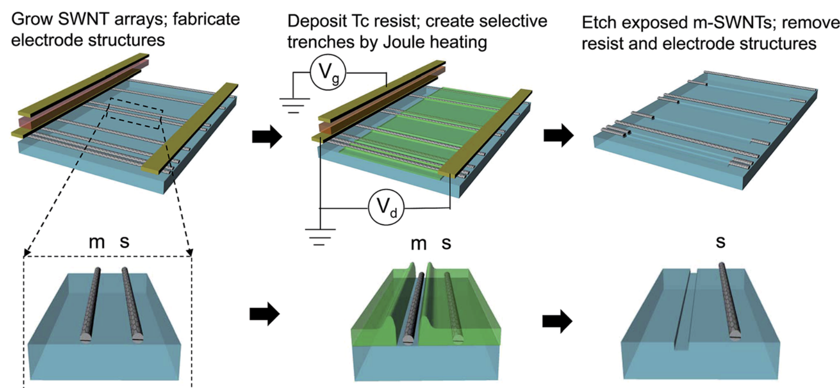

Fig. 1 Schematic illustration of the process for purifying arrays of SWNTs.

Published on 04 September 2014. Downloaded by Zhejiang University on 12/09/2014 01:10:14.

evaporation forms an ultrathin (~25 nm) amorphous film of a small-molecule organic species α,α,α′-tris(4-hydroxyphenyl)-1-ethyl-4-isopropylbenzene (*i.e.* MG2OH) on the top of SWNT arrays. The transistor structure allows injection of current and associated Joule heating only in m-SWNTs. This heating drives mass transport in the thin film and results in local trenches above the m-SWNTs. Reactive ion etching physically eliminates the m-SWNTs, which are all exposed in this manner, while leaving the s-SWNTs unaltered. Removing the thin film and electrode structures completes the process to yield arrays of only s-SWNTs in configurations well suited for planar integration into diverse classes of devices and sensors that demand, or benefit from, exclusively semiconducting operation. Fig. 2a shows an AFM image of a m-SWNT coated with thin film (~30 nm) after Joule heating (~1.77 μW μm^{-1}) with a substrate temperature of 348 K for 70 min. A typical cross-sectional trench profile extracted from experimental measurement is shown in Fig. 2b. The key parameters associated with the trench profile, trench width W_{Tc} and trench depth H_{Tc}, are also defined.

A full understanding of the physics associated with this process is critical for further optimization and use of this physics, not only in purification of SWNTs, but also in nanolithography, device fabrication and other areas as well. Our objective here is to develop an analytical model as well as a fully coupled thermo-mechanical-fluid finite element model to study this process. Although some major physics of the thermocapillary flow have been explored in Jin *et al.*'s work,[40] the focus of this paper, in addition to provide details of models, aims at establishing a scaling law for the trenches in terms of geometry parameters (*e.g.*, film thickness), material properties (*e.g.*, surface tension coefficient and viscosity) and loading parameters (*e.g.*, power density) to provide guidelines for optimizing the trench geometry, which is important for the formation of a s-SWNT array with large densities required in semiconducting applications.[39]

The paper is outlined as follows. The thermal modeling for temperature distribution is performed in Section 2, while the modeling of thermocapillary flow to form trenches is presented in Section 3. A scaling law for the thickness profile is established in Section 4. The results and discussion are given in Section 5.

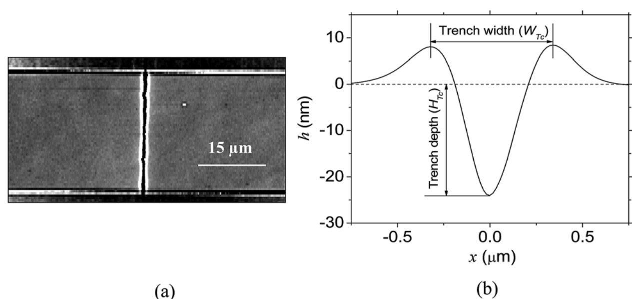

Fig. 2 (a) An AFM image of a SWNT coated with thin film (~30 nm) after Joule heating (~1.77 μW μm^{-1}) with substrate temperature 348 K for 70 min; (b) a typical cross-sectional trench profile extracted from experimental measurement.

2. Thermal modeling for temperature distribution

In this section, we describe procedures to determine the temperature distribution resulting from a SWNT embedded in a thin film of MG2OH with thickness h_{f} on a quartz substrate with power dissipation per unit length Q_0 as shown in Fig. 3a. Because the thickness of quartz substrate, ~10 mm, is much larger than that of film (~30 nm), it is modeled as a semi-infinite substrate. The origin of the coordinate system (x,y,z) is located at the center of the SWNT with x along the direction normal to the SWNT axis, y along the SWNT axis, and z pointing from quartz substrate to the MG2OH film. Due to the large aspect ratio of SWNT (*i.e.*, the length ~ 10 μm and the diameter ~ 1 nm), the SWNT can be modeled as an L-long line heat source. The resulting temperature rise is then obtained by integrating the one due to a point heat source, which is to be obtained below from the solution due to a circular disk heat source as shown in Fig. 3b. The temperature rise from the ambient temperature $\Delta T_{\mathrm{d}} = T_{\mathrm{d}} - T_{\infty}$ due to a circular disk heat source with radius r_0 satisfies the steady-state heat conduction equation

$$\frac{\partial^2 \Delta T_{\mathrm{d}}}{\partial r^2} + \frac{1}{r}\frac{\partial \Delta T_{\mathrm{d}}}{\partial r} + \frac{\partial^2 \Delta T_{\mathrm{d}}}{\partial z^2} = 0, \tag{1}$$

Published on 04 September 2014. Downloaded by Zhejiang University on 12/09/2014 01:10:14.

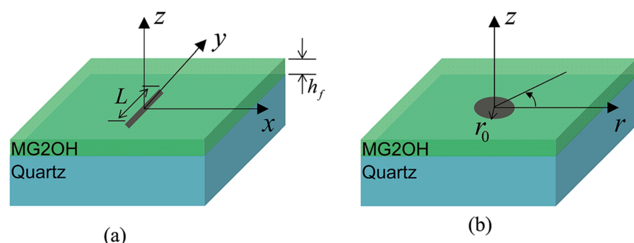

Fig. 3 The analytically modeled three-dimensional system with (a) a line and (b) a disk heat source at the interface between the film and the substrate for calculating the temperature distributions.

where (r,z) are the cylindrical coordinates with the origin at the center of the heat source (Fig. 3b).

The finite element analysis shows that the heat losses from radiation and convention are negligible. The top surface of film ($z = h_f$) can be assumed to be thermal insulation which gives

$$-k_f \frac{\partial \Delta T_d}{\partial z}\bigg|_{z=h_f} = 0, \quad (2)$$

where k_f is the thermal conductivity of thin film. Across the film/substrate interface ($z = 0$), the temperature is continuous

$$\Delta T_d|_{z=0^+} = \Delta T_d|_{z=0^-}, \quad (3)$$

and the heat flux is also continuous except the region of heat source ($z = 0$, $r \leq r_0$)

$$-k_f \frac{\partial \Delta T_d}{\partial z}\bigg|_{z=0^+} + k_s \frac{\partial \Delta T_d}{\partial z}\bigg|_{z=0^-} = \begin{cases} 0 & r > r_0 \\ \dfrac{P}{\pi {r_0}^2} & 0 \leq r \leq r_0 \end{cases}, \quad (4)$$

with k_s as the thermal conductivity of substrate and P as the total power of the disk heat source. The ambient temperature at the bottom surface of substrate ($z = -\infty$) gives

$$\Delta T_d|_{z=-\infty} = 0. \quad (5)$$

The Hankel transform $\Delta \overline{T}_d(\xi,z) = \int_0^\infty \Delta T_d(r,z) J_0(\xi r) r \mathrm{d}r$ of the steady-state heat conduction eqn (1) gives the following ordinary differential equation,

$$\frac{\mathrm{d}^2 \Delta \overline{T}_d}{\mathrm{d}z^2} - \xi^2 \Delta \overline{T}_d = 0, \quad (6)$$

where J_0 is the 0th order Bessel function of the first kind. The equation above has the solution

$$\Delta \overline{T}_d(\xi,z) = A(\xi)e^{-\xi z} + B(\xi)e^{\xi z}, \quad (7)$$

where $A(\xi)$ and $B(\xi)$ are to be determined with A_f and B_f for film, and A_s and B_s for the substrate, respectively. Performing the Hankel transform to the boundary and continuity conditions in eqn (2)–(5) yields

$$A_f e^{-\xi z} - B_f e^{\xi z} = 0, \quad (8)$$

$$A_f + B_f = A_s + B_s, \quad (9)$$

$$k_f \xi (A_f - B_f) - k_s \xi (A_s - B_s) = \frac{P J_1(\xi r_0)}{\pi r_0 \xi}, \quad (10)$$

$$A_s = 0, \quad (11)$$

where J_1 is the 1st-order Bessel function of the first kind. Solving eqn (8)–(11) yields

$$\begin{Bmatrix} A_f \\ B_f \\ A_s \\ B_s \end{Bmatrix} = \frac{P J_1(\xi r_0)}{2\pi k_s r_0 \xi^2 \left[\cosh(\xi h_f) + \dfrac{k_f}{k_s}\sinh(\xi h_f)\right]} \begin{Bmatrix} e^{\xi h_f} \\ e^{-\xi h_f} \\ 0 \\ 2\cosh(\xi h_f) \end{Bmatrix}. \quad (12)$$

The inverse Hankel transform $\Delta T_d(r,z) = \int_0^\infty \Delta \overline{T}_d(\xi,z) J_0(\xi r) \xi \mathrm{d}\xi$ then gives the temperature distributions in the film $\Delta T_d^f(r,z)$ and substrate $\Delta T_d^s(r,z)$ due to the disk heat source as

$$\Delta T_d^{film}(r,z) = \frac{P}{\pi k_s r_0} \int_0^\infty \frac{J_1(\xi r_0) J_0(\xi r) \cosh[\xi(h_f - z)]}{\xi \left[\cosh(\xi h_f) + \dfrac{k_f}{k_s}\sinh(\xi h_f)\right]} \mathrm{d}\xi, \quad (13)$$

$$\Delta T_d^{substrate}(r,z) = \frac{P}{\pi k_s r_0} \int_0^\infty \frac{J_1(\xi r_0) J_0(\xi r) \cosh(\xi h_f) e^{\xi z}}{\xi \left[\cosh(\xi h_f) + \dfrac{k_f}{k_s}\sinh(\xi h_f)\right]} \mathrm{d}\xi. \quad (14)$$

Taking the limit as the disk radius r_0 reduces to zero (*i.e.*, $J_1(\xi r_0)/r_0$ goes to $\xi/2$) yields the temperature rise in the film $\Delta T_p^f(r,z)$ and in the substrate $\Delta T_p^s(r,z)$ due to a point heat source as

$$\Delta T_p^{film}(r,z) = \frac{P}{2\pi k_s} \int_0^\infty \frac{J_0(\xi r) \cosh[\xi(h_f - z)]}{\cosh(\xi h_f) + \dfrac{k_f}{k_s}\sinh(\xi h_f)} \mathrm{d}\xi, \quad (15)$$

$$\Delta T_p^{substrate}(r,z) = \frac{P}{2\pi k_s} \int_0^\infty \frac{J_0(\xi r) \cosh(\xi h_f) e^{\xi z}}{\cosh(\xi h_f) + \dfrac{k_f}{k_s}\sinh(\xi h_f)} \mathrm{d}\xi. \quad (16)$$

For a point heat source at $(0,\eta,0)$ with heat generation $P = Q_0 \mathrm{d}\eta$, the integration of eqn (15) and (16) with $r = \sqrt{x^2 + (\eta - y)^2}$ gives the temperature rise at point (x,y,z) due to a line heat source as

$$\Delta T^{film}(x,y,z) = \frac{Q_0}{2\pi k_s} \int_{-L/2}^{L/2} \mathrm{d}\eta \int_0^\infty \frac{J_0\left(\xi\sqrt{x^2 + (\eta - y)^2}\right) \cosh[\xi(h_f - z)]}{\cosh(\xi h_f) + \dfrac{k_f}{k_s}\sinh(\xi h_f)} \mathrm{d}\xi, \quad (17)$$

 This journal is © The Royal Society of Chemistry 2014

Published on 04 September 2014. Downloaded by Zhejiang University on 12/09/2014 01:10:14.

$$\Delta T^{\text{substrate}}(x,y,z) = \frac{Q_0}{2\pi k_s}\int_{-L/2}^{L/2} \mathrm{d}\eta \int_0^{\infty} \frac{J_0\left(\xi\sqrt{x^2+(\eta-y)^2}\right)\cosh(\xi h_f)\mathrm{e}^{\xi z}}{\cosh(\xi h_f)+\dfrac{k_f}{k_s}\sinh(\xi h_f)}\mathrm{d}\xi. \tag{18}$$

It should be noted that the temperature rise is proportional to the power density applied in the SWNT. The temperature rise on the surface ($z = h_f$) of thin film to be used in the modeling of thermocapillary flow in Section 3 is then given by

$$\Delta T_{\text{surface}}(x,y) = \frac{Q_0}{2\pi k_s}\int_{-L/2}^{L/2} \mathrm{d}\eta \int_0^{\infty} \frac{J_0\left(\xi\sqrt{x^2+(\eta-y)^2}\right)}{\cosh(\xi h_f)+\dfrac{k_f}{k_s}\sinh(\xi h_f)}\mathrm{d}\xi. \tag{19}$$

A three-dimensional finite element model is also established to study the temperature distribution in the system and validate the analytical model. Eight-node, hexahedral brick elements in the finite element software ABAQUS are used to discretize the geometry (including film, substrate and SWNT). Due to the symmetries of the system, only a quarter model is considered. A volume heat source is applied on the SWNT. The zero heat flux boundary is applied at the top surface of the film, and a constant temperature T_∞ is applied at the bottom of the quartz substrate. The lateral dimension ($\sim$10 μm × 50 μm) of the system and the substrate thickness ($\sim$500 μm) are taken as large enough to ensure the accuracy of the results.

3. Modeling of thermocapillary flow

The motion of the thermocapillary flow in thin film can be approximated as unidirectional since the SWNT length ($L \sim 30$ μm) is much larger than its diameter ($\sim$1.0 nm). As shown in Fig. 4, a two dimensional model is established for the thickness profile $h(x,t)$ by following the approach of Darhuber *et al.*[41] to assume the thin film as a Newtonian liquid with the Navier–Stokes equations reduced to

$$\frac{\partial p}{\partial x} = \mu\frac{\partial^2 u}{\partial z^2},\ \frac{\partial p}{\partial z} = 0 \tag{20}$$

where $u(x,z,t)$ is the velocity along x direction, p is the pressure and μ is the film viscosity. Local heating of a liquid film at a position x reduces the surface tension $\gamma(x)$, which usually depends linearly on the surface temperature of film [*i.e.*, $\gamma = \gamma_0 - \gamma_1\Delta T_{\text{surface}}(x)$ with γ_0 as the surface tension at $T = T_\infty$ and γ_1 the temperature coefficient of surface tension], to produce a thermocapillary shear stress

$$\tau = \frac{\mathrm{d}\gamma}{\mathrm{d}x} = -\gamma_1\frac{\mathrm{d}\Delta T_{\text{surface}}(x)}{\mathrm{d}x}, \tag{21}$$

at the air–liquid interface, which pulls liquid toward regions of cooler surface. The surface temperature $\Delta T_{\text{surface}}(x)$ is given from eqn (19) by setting $y = 0$, *i.e.*,

$$\Delta T_{\text{surface}}(x) = \frac{Q_0}{2\pi k_s}\int_{-L/2}^{L/2} \mathrm{d}\eta \int_0^{\infty} \frac{J_0\left(\xi\sqrt{x^2+\eta^2}\right)}{\cosh(\xi h_f)+\dfrac{k_f}{k_s}\sinh(\xi h_f)}\mathrm{d}\xi. \tag{22}$$

The boundary conditions are given by

$$u(x,z=0,t)=0,\ \ \mu\frac{\partial u}{\partial z}(x,z=h,t)=\tau \tag{23}$$

which corresponds to non-slip condition at the liquid-solid (*i.e.*, film/substrate) interface and a shear stress at the liquid–air interface. For the thickness profile with small slopes, the pressure can be written as

$$p(x,t) = -\gamma\frac{\partial^2 h}{\partial x^2}, \tag{24}$$

Solving eqn (20), (23) and (24) yields the velocity

$$u(x,z,t) = \frac{1}{\mu}\left[\gamma\frac{\partial^2 h}{\partial x^2}\left(zh(x,t)-\frac{z^2}{2}\right)+\tau z\right], \tag{25}$$

The kinematic condition requires dh/dt being equal to the surface flow speed normal to the air–liquid interface and leads to the evolution equation for the film thickness,

$$\frac{\partial h}{\partial t}+\frac{\mathrm{d}Q}{\mathrm{d}x}=0, \tag{26}$$

where $Q = \int_0^h u(x,z,t)\mathrm{d}z$ is the volumetric flow rate per unit length. Therefore, the governing equation for the film thickness is obtained as

$$\frac{\partial h}{\partial t}+\frac{\partial}{\partial x}\left[\frac{\tau h^2}{2\mu}+\frac{h^3}{3\mu}\frac{\partial}{\partial x}\left(\gamma\frac{\partial h^2}{\partial x^2}\right)\right]=0, \tag{27}$$

with boundary conditions $h(\pm\infty,t) = h_f$ and $\partial^2 h/\partial x^2(\pm\infty,t) = 0$ (zero pressure), and initial condition $h(x,t=0) = h_f$.

A two-dimensional fully coupled thermo-mechanical-fluid finite element model is developed using COMSOL to validate the above analytical model. The thin film is modeled as a Newtonian liquid while the substrate and SWNT are solid. A volume heat source is applied on the SWNT. The boundary

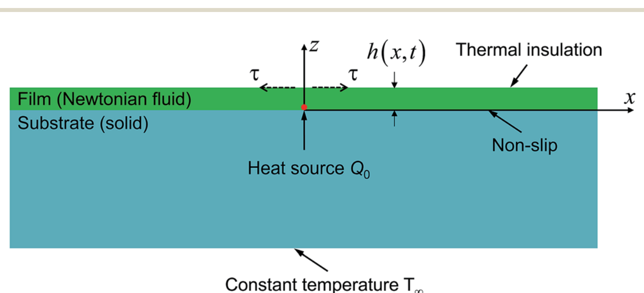

Fig. 4 The schematic diagram of the two-dimensional system for the thermocapillary flow modeling.

Published on 04 September 2014. Downloaded by Zhejiang University on 12/09/2014 01:10:14.

conditions for heat transfer include a constant temperature T_∞ at the bottom of substrate and heat insulations at other boundaries. Surface tension with the form of $\gamma = \gamma_0 - \gamma_1 \Delta T_{\text{surface}}(x)$ is applied on the top surface of thin film and a non-slip boundary is applied at the interface of film and substrate. The lateral dimension is taken as a few tens micrometers (~50 μm) and the substrate thickness (~500 μm) to ensure the accurate calculation. The diameter of SWNT is set as 2 nm. It should be noted that this two-dimensional model for thermocapillary flow yields a temperature change as the thickness profile evolves to form a trench while the temperature [eqn (22)] used in the analytical model is assumed to be independent of the thickness profile. This assumption is well validated by the good agreement among the analytical prediction of the thickness profile, the finite element simulations and experiments, which are shown in Section 5.

4. A scaling law for the thickness profile

The thickness profile in eqn (27) are very complex since it depends on multiple material parameters (*e.g.*, viscosity μ, surface tension γ, thermal conductivities k_f and k_s), geometry parameter (*e.g.*, film thickness h_f) and loading parameter (*e.g.*, power per unit length Q_0). In this section, we will establish a simple scaling law to show clearly the influences of various parameters on the thickness profile.

By introducing the non-dimensional terms $\overline{\Delta T_{\text{surface}}} = k_s \Delta T_{\text{surface}}/Q_0$, $\bar{x} = x/h_f$, $\bar{\xi} = \xi h_f$, and $\bar{\eta} = \eta/h_f$, the surface temperature rise in eqn (22) can be written in the non-dimensional form as

$$\overline{\Delta T_{\text{surface}}}(\bar{x}) = \frac{1}{2\pi}\int_{-L/(2h_f)}^{L/(2h_f)} \mathrm{d}\bar{\eta}\int_0^\infty \frac{J_0\left(\bar{\xi}\sqrt{\bar{x}^2+\bar{\eta}^2}\right)}{\cosh(\bar{\xi}) + \frac{k_f}{k_s}\sinh(\bar{\xi})}\mathrm{d}\bar{\xi}. \quad (28)$$

Since the SWNT length (~30 μm) is much larger than the film thickness (~25 nm), L/h_f can be approximated as infinity, which yields a simple scaling law for the surface temperature rise such that the normalized surface temperature rise $k_s\Delta T_{\text{surface}}/Q_0$ depends on only one non-dimensional parameter: the normalized thermal conductivity k_f/k_s, *i.e.*,

$$\overline{\Delta T_{\text{surface}}} = \frac{k_s}{Q_0}\Delta T_{\text{surface}} = \overline{\Delta T_{\text{surface}}}\left(\bar{x}; \frac{k_f}{k_s}\right). \quad (29)$$

Let $\bar{h} = h/h_f$, $\bar{t} = \gamma_1 Q_0 t/(\mu_0 k_s h_f)$, $\bar{\mu} = \mu/\mu_0$, $\bar{\tau} = -\mathrm{d}\overline{\Delta T_{\text{surface}}}/\mathrm{d}\bar{x}$ and $\bar{\gamma} = k_s\gamma/(Q_0\gamma_1) = k_s\gamma_0/(Q_0\gamma_1) - \overline{\Delta T_{\text{surface}}}$ with μ_0 as the viscosity at $T = T_\infty$ and μ the viscosity at T. Eqn (27) can then be written in the non-dimensional form as

$$\frac{\partial \bar{h}}{\partial \bar{t}} + \frac{\partial}{\partial \bar{x}}\left\{-\frac{\bar{h}^2}{2\bar{\mu}}\frac{\mathrm{d}\overline{\Delta T_{\text{surface}}}}{\mathrm{d}\bar{x}} + \frac{\bar{h}^3}{3\bar{\mu}}\frac{\partial}{\partial \bar{x}}\left[\left(\frac{k_s\gamma_0}{Q_0\gamma_1} - \overline{\Delta T_{\text{surface}}}\right)\frac{\partial^2 \bar{h}}{\partial \bar{x}^2}\right]\right\} = 0, \quad (30)$$

which yields a simple scaling law for the thickness profile such that the normalized thickness profile depends on only three non-dimensional parameters: the normalized viscosity $\bar{\mu}$, the normalized thermal conductivity k_f/k_s and $\frac{k_s\gamma_0}{Q_0\gamma_1}$, *i.e.*,

$$\bar{h} = \frac{h}{h_f} = \bar{h}\left(\bar{x}, \bar{t}; \bar{\mu}, \frac{k_f}{k_s}, \frac{k_s\gamma_0}{Q_0\gamma_1}\right), \quad (31)$$

5. Results and discussion

Fig. 5 shows the dependence of the normalized surface temperature distribution $k_s\Delta T_{\text{surface}}/Q_0$ in eqn (28) on the normalized thermal conductivity k_f/k_s. We take two values of the normalized thermal conductivity ($k_f/k_s = 1/30$ for MG2OH/quartz and 1.0) to show its effect. The result from the three-dimensional finite element model for $k_f/k_s = 1/30$ is also shown for comparison. The good agreement validates the analytical expression for the surface temperature rise in eqn (28). It is shown that the surface temperature rise as well as the temperature gradient due to Joule heating is localized within a range of 5 times film thickness ($x < 5h_f$), which is critical to form a local trench. The maximum normalized temperature rise occurs at the center of SWNT (*i.e.*, $x = 0$) while the maximum normalized temperature gradient occurs at the location of one time thickness (*i.e.*, $x = h_f$). The increase of k_f/k_s decreases both the normalized temperature rise and temperature gradient locally in the range of 5 times thickness ($x < 5h_f$) but has a negligible effect on the results out of that range ($x > 5h_f$). For example, as k_f/k_s increases 1/30 to 1, the maximum temperature rise decreases ~10% at $x = 0$ and ~0.8% at $x = 5h_f$.

Let's focus on the system of MG2OH on a quartz substrate in Jin *et al.*'s work to purify the SWNTs,[40] the thermal conductivities of MG2OH film and quartz substrate are $k_f = 0.2$ W m^{-1} K^{-1} and $k_s = 6$ W m^{-1} K^{-1},[40,42] respectively, which gives $k_f/k_s = 1/30$. The film thickness is ~25 nm. The maximum normalized surface temperature rise $(\overline{\Delta T_{\text{surface}}})_{\max}$ and temperature gradient $(\mathrm{d}\overline{\Delta T_{\text{surface}}}/\mathrm{d}\bar{x})_{\max}$ are obtained from Fig. 5 as 2.49 and −0.27, respectively, which gives a small maximum surface temperature $(\Delta T_{\text{surface}})_{\max} = 4.15$ K but a large temperature gradient $(\mathrm{d}\Delta T_{\text{surface}}/\mathrm{d}x)_{\max} = -1.77 \times 10^7$ K m^{-1} (sufficiently large to drive thermocapillary flow of film to form trenches) for the power density on the order of ~10 W m^{-1} in experiments. The small rise in surface temperature (only in a few degrees) yields a small change in viscosity and therefore, $\bar{\mu} \approx 1$. Eqn (31) then becomes

$$\bar{h} = \frac{h}{h_f} = \bar{h}\left(\bar{x}, \bar{t}; \bar{\mu} \approx 1, \frac{k_f}{k_s} = \frac{1}{30}, \frac{k_s\gamma_0}{Q_0\gamma_1}\right), \quad (32)$$

which only depends on one non-dimensional parameter $\frac{k_s\gamma_0}{Q_0\gamma_1}$.

Fig. 6 compares the predicted thickness profile to the two-dimensional fully coupled thermo-mechanical-fluid analysis for $\frac{k_s\gamma_0}{Q_0\gamma_1} = 245$. The good agreement between analytical modeling and numerical simulations for $\bar{t} = 40$ and $\bar{t} = 400$ validates the analytical model although several assumptions are

 This journal is © The Royal Society of Chemistry 2014

Published on 04 September 2014. Downloaded by Zhejiang University on 12/09/2014 01:10:14.

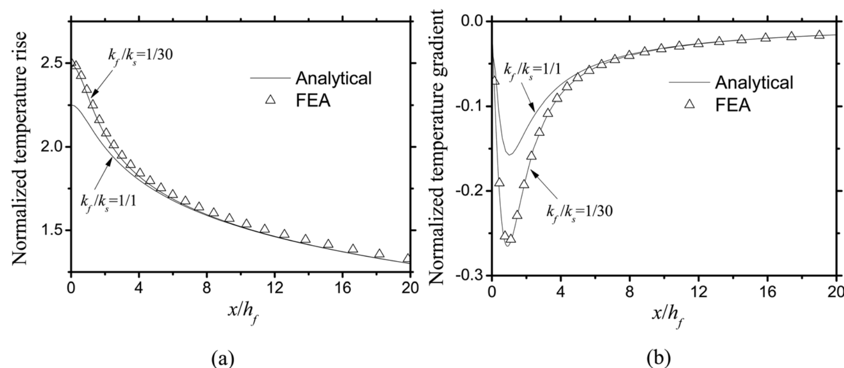

Fig. 5 The distribution of the normalized (a) temperature rise and (b) temperature gradient at the top surface of thin film.

introduced in the modeling (*e.g.*, the independence of the temperature on the thermocapillary flow). As the time increases, the trenches gradually widen and deepen as the displacement material forms ridges at the edges. It should be noted that the viscosity doesn't play a role in determining the thickness profile but it could accelerate or decelerate the trench formation time since it appears in the normalized time.

The dependence of the normalized trench width $W_{\mathrm{Tc}}/h_{\mathrm{f}}$ and trench depth $H_{\mathrm{Tc}}/h_{\mathrm{f}}$ on the non-dimensional parameter $\frac{k_{\mathrm{s}}\gamma_0}{Q_0\gamma_1}$ is shown in Fig. 7. A smaller $\frac{k_{\mathrm{s}}\gamma_0}{Q_0\gamma_1}$ gives a larger normalized trench depth but not always for the normalized trench width. When the normalized time is small (<5), the normalized trench width is independent of the normalized parameter $\frac{k_{\mathrm{s}}\gamma_0}{Q_0\gamma_1}$. When the normalized time is large (>5), the normalized trench width shows a similar dependence on $\frac{k_{\mathrm{s}}\gamma_0}{Q_0\gamma_1}$ as the normalized trench depth. The above conclusions agree very well with experimental observation.[40] To further understand the effect of the unique parameter $\frac{k_{\mathrm{s}}\gamma_0}{Q_0\gamma_1}$ on the trench profile, we redraw the results in Fig. 7 as 8 of the normalized trench width *versus* the normalized trench depth. The normalized full trench width corresponding to the normalized full trench depth (*i.e.*, $H_{\mathrm{Tc}}/h_{\mathrm{f}} = 1$) is critical to form a s-SWNT array with large densities required in semiconducting applications. The results suggest that a smaller $\frac{k_{\mathrm{s}}\gamma_0}{Q_0\gamma_1}$ is helpful to generate a narrower normalized full trench width, which can serve as a guideline for optimizing the system. In addition, a thinner film thickness is also helpful for a narrower full trench width since the full trench width is proportional to the film thickness.

Due to limited data on viscosity and surface tension of MG2OH, we take the surface tension of polystyrene (*i.e.*, $\gamma = 50.40 \times 10^{-3} - 0.0738 \times 10^{-3}\Delta T_{\mathrm{surface}}(x)$ N m^{-1}),[43] which exhibits behaviors like the MG2OH, as an approximation and fit the viscosity μ_0 to compare with experimental measurement.

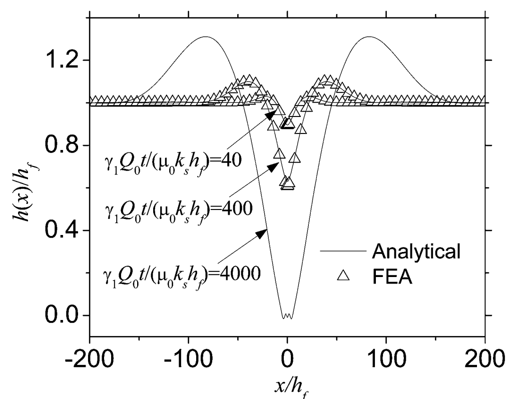

Fig. 6 Evolution of the trench profile.

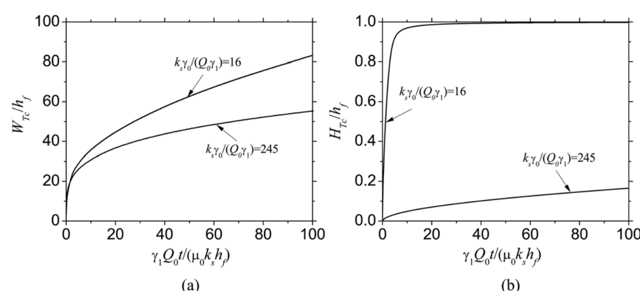

Fig. 7 The normalized (a) trench width and (b) trench depth *versus* the normalized time.

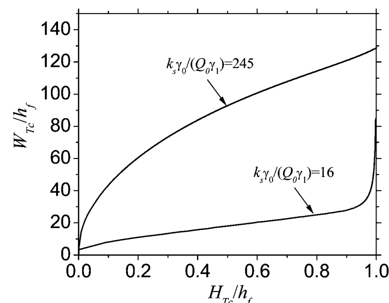

Fig. 8 The normalized trench width *versus* the normalized trench depth.

Published on 04 September 2014. Downloaded by Zhejiang University on 12/09/2014 01:10:14.

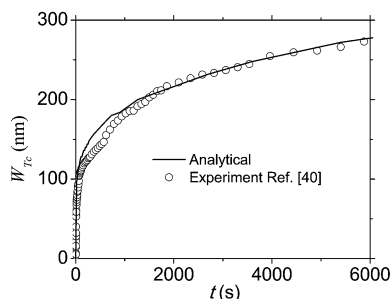

Fig. 9 The trench width *versus* time.

Fig. 9 shows the comparison of the trench width *versus* time between the analytical prediction and experiments for the power density 16.7 W m^{-1} and ambient temperature $T_\infty = 303$ K. The fitted viscosity μ_0 is 4×10^8 Pa·s at 303 K. These results indicate a novel measurement technique for quantifying the viscosity of thin film.

6. Conclusions

We have developed an analytical model, validated by the coupled thermo-mechanical-fluid finite element analysis, to study the thermocapillary flow of thin film to purify the SWNTs. A simple scaling law for the normalized thickness profile shows that the normalized thickness during thermocapillary motion depends only on three non-dimensional parameters: the normalized viscosity μ/μ_0, the normalized thermal conductivity k_f/k_s and $\frac{k_s\gamma_0}{Q_0\gamma_1}$, where μ_0 is the viscosity at the ambient temperature, k_f and k_s are the thermal conductivities of thin film and substrate, respectively, Q_0 is the power density on SWNTs, γ_0 is the surface tension of thin film at the ambient temperature, and γ_1 is the temperature coefficient of surface tension. For the system of MG2OH/quartz substrate under a low power density, the normalized thickness profile only depends on one non-dimensional parameter $\frac{k_s\gamma_0}{Q_0\gamma_1}$. A smaller $\frac{k_s\gamma_0}{Q_0\gamma_1}$ is helpful to yield a narrower full trench width. In addition, a thinner film thickness is also helpful for a narrower full trench width. These may serve as design guidelines for system optimization.

Acknowledgements

J.S. acknowledges the supports from the National Natural Science Foundation of China (Grant nos. 11372272 and 11321202), the Fundamental Research Funds for the Central Universities (2014FZA4027), and the Thousand Young Talents Program of China. C.L. acknowledges the supports from the National Natural Science Foundation of China (Grant nos. 11172263 and 11322216) and the Zhejiang Provincial Natural Science Foundation of China (Grant no. LR13A020001).

References

1 P. Avouris, Z. Chen and V. Perebeinos, *Nat. Nanotechnol.*, 2007, **2**, 605–615.
2 S. J. Kang, C. Kocabas, T. Ozel, M. Shim, N. Pimparkar, M. A. Alam, S. V. Rotkin and J. A. Rogers, *Nat. Nanotechnol.*, 2007, **2**, 230–236.
3 C. Wang, K. Takei, T. Takahashi and A. Javey, *Chem. Soc. Rev.*, 2013, **42**, 2592–2609.
4 M. M. Shulaker, G. Hills, N. Patil, H. Wei, H. Y. Chen, H. S. P. Wong and S. Mitra, *Nature*, 2013, **501**, 526–530.
5 A. D. Franklin, M. Luisier, S. J. Han, G. Tulevski, C. M. Breslin, L. Gignac, M. S. Lundstrom and W. Haensch, *Nano Lett.*, 2012, **12**, 758–762.
6 L. Ding, Z. Zhang, S. Liang, T. Pei, S. Wang, Y. Li, W. Zhou, J. Liu and L. M. Peng, *Nat. Commun.*, 2012, **3**, 677.
7 A. D. Franklin, S. O. Koswatta, D. B. Farmer, J. T. Smith, L. Gignac, C. M. Breslin, S. J. Han, G. S. Tulevshi, H. Miyazoe, W. Haensch and J. Tersoff, *Nano Lett.*, 2013, **13**, 2490–2495.
8 J. Zhang, A. Lin, N. Patil, H. Wei, L. Wei, H. S. P. Wong and S. Mitra, *IEEE Transactions on Computer-Aided Design*, 2012, **31**, 453–471.
9 H. Park, A. Afzali, S. J. Han, G. S. Tulevski, A. D. Franklin, J. Tersoff, J. B. Hannon and W. Haensch, *Nat. Nanotechnol.*, 2012, **7**, 787–791.
10 S. J. Choi, P. Bennett, K. Takei, C. Wang, C. C. Lo, A. Javey and J. Bokor, *ACS Nano*, 2013, **7**, 798–803.
11 C. Kocabas, H. S. Kim, T. Banks, J. A. Rogers, A. A. Pesetski, J. E. Baumgardner, S. V. Krishnaswamy and H. Zhang, *Proc. Natl. Acad. Sci. U. S. A.*, 2008, **105**, 1405–1409.
12 M. Steiner, M. Engel, Y. M. Lin, Y. Wu, K. Jenkins, D. B. Farmer, J. J. Humes, N. L. Yoder, J. W. T. Seo, A. A. Green, M. C. Hersam, R. Krupke and P. Avouris, *Appl. Phys. Lett.*, 2012, **101**, 053123.
13 C. Wang, A. Badmaev, A. Jooyaie, M. Bao, K. L. Wang, K. Galatsis and C. Zhou, *ACS Nano*, 2011, **5**, 4169–4176.
14 Q. Cao, S. J. Han, G. S. Tulevski, Y. Zhu, D. D. Lu and W. Haensch, *Nat. Nanotechnol.*, 2013, **8**, 180–186.
15 L. Nougaret, H. Happy, G. Dambrine, V. Deryche, J. P. Bourgoin, A. A. Green and M. C. Hersam, *Appl. Phys. Lett.*, 2009, **94**, 243505.
16 C. Rutherglen, D. Jain and P. Burke, *Nat. Nanotechnol.*, 2009, **4**, 811–819.
17 X. Xie, A. E. Islam, M. A. Wahab, L. Ye, X. Ho, M. A. Alam and J. A. Rogers, *ACS Nano*, 2012, **6**, 7981–7988.
18 P. Avouris, M. Freitag and V. Perebeinos, *Nat. Photonics*, 2008, **2**, 341–350.
19 L. Yang, S. Wang, Q. Zeng, Z. Zhang, T. Pei, Y. Li and L. M. Peng, *Nat. Photonics*, 2011, **5**, 672–676.
20 M. E. Roberts, M. C. LeMieux and Z. N. Bao, *ACS Nano*, 2009, **3**, 3287–3293.
21 B. L. Allen, P. D. Kichambare and A. Star, *Adv. Mater.*, 2007, **19**, 1439–1451.
22 P. Qi, O. Vermesh, M. Grecu, A. Javey, Q. Wang, H. Dai, S. Peng and K. J. Cho, *Nano Lett.*, 2013, **3**, 347–351.

 This journal is © The Royal Society of Chemistry 2014

Published on 04 September 2014. Downloaded by Zhejiang University on 12/09/2014 01:10:14.

23 C. Kocabas, S. H. Hur, A. Gaur, M. A. Meitl, M. Shim and J. A. Rogers, *Small*, 2005, **1**, 1110–1116.

24 M. S. Arnold, A. A. Green, J. F. Hulvat, S. I. Stupp and M. C. Hersam, *Nat. Nanotechnol.*, 2006, **1**, 60–65.

25 A. A. Green and M. C. Hersam, *Adv. Mater.*, 2011, **23**, 2185–2190.

26 M. Zheng and E. D. Semke, *J. Am. Chem. Soc.*, 2007, **129**, 6084–6085.

27 H. Liu, D. Nishide, T. Tanaka and H. Kataura, *Nat. Commun.*, 2011, **2**, 1–8.

28 J. Wu, L. Xie, G. Hong, H. E. Lim, B. Thendie, Y. Miyata, H. Shinohara and H. Dai, *Nano Res.*, 2012, **5**, 388–394.

29 R. Krupke, F. Hennrich, H. van Löhneysen and M. M. Kappes, *Science*, 2003, **301**, 344–347.

30 X. Li, L. Zhang, X. Wang, I. Shimoyama, X. Sun, W. S. Seo and H. Dai, *J. Am. Chem. Soc.*, 2007, **129**, 4890–4891.

31 M. Engel, J. P. Small, M. Steiner, M. Freitag, A. A. Green, M. C. Hersam and P. Avouris, *ACS Nano*, 2008, **2**, 2445–2452.

32 M. C. LeMieux, M. Roberts, S. Barman, Y. W. Jin, J. M. Kim and Z. Bao, *Science*, 2008, **321**, 101–104.

33 J. Xiao, S. Dunham, P. Liu, Y. Zhang, C. Kocabas, L. Moh, Y. Huang, K. C. Hwang, C. Liu, W. Huang and J. A. Rogers, *Nano Lett.*, 2009, **9**, 4311–4319.

34 P. G. Collins, M. S. Arnold and P. Avouris, *Science*, 2001, **292**, 706–709.

35 K. Balasubramanian, R. Sordan, M. Burghard and K. Kern, *Nano Lett.*, 2004, **4**, 827–830.

36 S. Banerjee and S. S. Wong, *Nano Lett.*, 2004, **4**, 1445–1450.

37 H. Hu, B. Zhao, M. A. Hamon, K. Kamaras, M. E. Itkis and R. C. Haddon, *J. Am. Chem. Soc.*, 2003, **125**, 14893–14900.

38 H. Huang, R. Maruyama, K. Noda, H. Kajiura and K. Kadono, *J. Phys. Chem. B*, 2006, **110**, 7316–7320.

39 A. D. Franklin, *Nature*, 2013, **498**, 443.

40 S. H. Jin, S. N. Dunham, J. Song, X. Xie, J. H. Kim, C. Lu, A. Islam, F. Du, J. Kim, J. Felts, Y. Li, F. Xiong, M. A. Wahab, M. Menon, E. Cho, K. L. Grosse, D. J. Lee, H. U. Chung, E. Pop, M. A. Alam, W. P. King, Y. Huang and J. A. Rogers, *Nat. Nanotechnol.*, 2013, **8**, 347–355.

41 A. A. Darhuber, J. M. Davis and S. M. Troian, *Phys. Fluids*, 2003, **15**, 1295–1304.

42 A. E. Beck, D. M. Darbha and H. H. Schloessin, *Phys. Earth Planet. Inter.*, 1978, **17**, 35–53.

43 M. Wulf, S. Michel, W. Jenschke, P. Uhlmann and K. Grundke, *Phys. Chem. Chem. Phys.*, 1999, **1**, 3899–3903.

This journal is © The Royal Society of Chemistry 2014